Author/s:
Best, SP;Streltsov, VA;Chantler, CT;Li, W;Ash, PA;Hayama, S;Diaz-Moreno, S

Title:
Redox state and photoreduction control using X-ray spectroelectrochemical techniques: advances in design and fabrication through additive engineering

Date:
2021-03-01

Citation:
Best, S. P., Streltsov, V. A., Chantler, C. T., Li, W., Ash, P. A., Hayama, S. & Diaz-Moreno, S. (2021). Redox state and photoreduction control using X-ray spectroelectrochemical techniques: advances in design and fabrication through additive engineering. Journal of Synchrotron Radiation, 28 (2), pp.472-479. https://doi.org/10.1107/s1600577520016021.

Persistent Link:
https://hdl.handle.net/11343/261668

Redox State and Photoreduction Control using X-ray Spectroelectrochemical Techniques – Advances in Design and Fabrication Through Additive Engineering

Authors

Stephen Peter Best[a]*, Victor A. Streltsov[b], Christopher Thomas Chantler[c], Wangzhe Li[d], Philip A. Ash[e], Shusaku Hayama[f] and Sofia Diaz-Moreno[f]
[a]School of Chemistry, The University of Melbourne, Parkville, Melbourne, Victoria, 3010, Australia
[b]Florey Department of Neuroscience and Mental Health, The University of Melbourne, Melbourne, Victoria, 3010, Australia
[c]School of Physics, The University of Melbourne, Melbourne, Victoria, 3010, Australia
[d]Department of Chemistry, University of Oxford, Oxford, Oxfordshire, OX1 3QR, UK
[e]Department of Chemistry, University of Leicester, Leicester, Leicestershire, LE1 7RH, UK
[f] Diamond Light Source, Didcot, Oxfordshire, OX11 0DE, UK

Correspondence email: spbest@unimelb.edu.au

Synopsis The design and operation of a 3D-printed flow in-situ electrochemical cell suitable for ambient temperature XAS measurements is described. The ability to control, and significantly limit, photoreduction whilst requiring only small solution volumes make this a superior sampling approach to cryogenic techniques for many samples.

Abstract The design and performance of an electrochemical cell and solution flow system optimised for the collection of X-ray absorption spectra from solutions of species sensitive to photodamage is described. A combination of 3D-CAD and 3D-printing techniques facilitate highly optimised design with low unit cost and short production time. Precise control of the solution flow is critical both to minimising the volume of solution needed and the minimisation of photodamage during data acquisition. The details of an integrated four-syringe stepper-motor driven pump and associated software are described. It is shown that combined electrochemical and flow control can allow repeated measurement of a defined volume of solution, 100 μL, of samples sensitive to photoreduction without significant change to the X-ray absorption near-edge structure and is demonstrated by measurements of copper(II) complexes. The flow *in-situ* electrochemical cell allows the collection of high-quality X-ray spectral measurements both in the near-edge region and over an extended energy region as is needed for structural analysis from solution samples. This approach provides control over photodamage at a level at least comparable to that achieved using cryogenic techniques and at the same time eliminates problems associated with interference due to Bragg peaks.

Keywords: XAS, XANES, Electrochemistry, spectroelectrochemistry, photoreduction, copper complexes, CAD design, Additive engineering, 3-D printing

1. Introduction

Structure elucidation of non-crystalline samples using X-ray absorption spectroscopy (XAS), from analysis of the X-ray near edge structure (XANES) or extended X-ray absorption fine structure (EXAFS) regions of the spectrum, plays a critical part in the understanding of materials where the property of interest is associated with an element which exclusively occurs at a specific site (Frenkel & van Bokhoven, 2014, Bunker, 2010, Parsons *et al.*, 2002). If the element has a moderate atomic number, then the X-ray energy is highly penetrating and highly specific results can be obtained from dilute samples. Metalloproteins present a matrix comprised mainly of low atomic number elements where protein function is often associated with a transition metal. If present in a single site, the coordination of the metal can be determined with greater precision using EXAFS than for many protein X-ray structures (Zhang, 2019, Tamura *et al.*, 2013, Cotelesage *et al.*, 2012, Shima *et al.*, 2008, Grunwaldt & Clausen, 2002, Zhang *et al.*, 1999) and this advantage can be extended to small molecule structure determination when the analysis incorporates data corrected for systematic errors with statistically-valid error propagation (Trevorah *et al.*, 2020, Schalken & Chantler, 2018, Bourke *et al.*, 2016).

Since there is not a requirement for crystalline samples, EXAFS permits structure determination of solvated species under conditions relevant to their function. This is particularly important for polypeptides where protein folding or acid/base reactions of the sidechains can impact on the active site structure. Despite the opportunity to make measurements from samples in the solution state, practical considerations have largely contributed to the predominance of XAS measurements from metalloproteins and related samples to be conducted from frozen samples, generally at temperatures well below that of liquid nitrogen. For measurements from first-row transition metals at the K edge, photoreduction can destroy the integrity of the sample on a timescale shorter than that needed for the measurement of an absorption spectrum. The impact of unwanted photoredox chemistry is particularly pronounced for solution samples at ambient temperatures, owing to diffusion of the primary and secondary products of photoionization. These problems may be addressed by employing solution jets, where reports of L-edge spectra (Kubin *et al.*, 2018) and XFEL (Chatterjee *et al.*, 2019) measurements give a measure of the current status. Even with highly optimised drop-on-demand approaches sample volumes of *ca.* 5 mL per spectrum are needed (Chatterjee *et al.*, 2019). Rapid freezing of the solution, after addition of cryoprotectants designed to reduce crystallisation, reduces significantly the sample volume requirements and can produce a sample which is more robust in terms of photoreduction, although problems commonly persist for absorbers such as Cu, As and Se (George *et al.*, 2012). This is well illustrated by recent studies into the impact of photoreduction of Cu-bound amyloid β peptide (CuAß) samples have examined both the time/flux dependence of sample degradation and the impact of cryoprotectants (Summers *et al.*, 2019, Stellato *et al.*, 2019, Streltsov *et al.*, 2008).

Against this backdrop we have sought to develop methods which allow the measurement of XAS spectra at hard X-ray energies (> 4 keV) from small-volumes (< 1 mL) of solution samples at ambient temperature under potentiostatic control. Early reports of the sulfur K-edge and molybdenum L-edge EXAFS of static N-methyl formamide solutions of the iron-molybdenum cofactor of nitrogenase (340 µL) under electrochemical control demonstrate the feasibility of the approach, albeit for samples which are stable over the long electrosynthesis timeframe (10 min) timescale and are not sensitive to photodamage (Schultz *et al.*, 1993). More recently we have described a small-volume flow electrochemical cell which is suitable for biological samples, *e.g.* cytochrome *c* (Best *et al.*, 2016) and for radiation-sensitive CuAß complexes (Streltsov *et al.*, 2018). A limitation to the more widespread use of that approach is the requirement for significant workshop facilities for the implementation of that design. Advances in additive manufacturing (3D printing) when coupled with CAD (computer assisted design) packages provide a path to more highly optimised cell designs which can be fabricated at low cost. In this contribution we describe the CAD-based design and 3D-printed XAS spectroelectrochemical (XAS-SEC) cells and the design and software control of an integrated stepper motor syringe pump. We also explore the strategies that these methods bring to the control of the redox state of the sample and demonstrate the data quality obtained using XAS-SEC methods.

2. Experimental

X-ray absorption spectra were measured using the I20-Scanning wiggler beamline of the Diamond Light Source (DLS) (Diaz-Moreno *et al.*, 2018). The four-bounce monochromator (Hayama *et al.*, 2018) equipped with Si(111) crystals gives an energy resolution, ΔE/E, better than 1.4×10^{-4} with a flux > 10^{12} ph/s and a focal spot size at the sample position of 0.4×0.3 mm^2 (H×V) FWHM. A Canberra 64-pixel Monolithic Segmented Hyper Pure Germanium Detector (HPGe) partnered with the Xspress4 digital pulse processor (Dennis *et al.*, 2019) was used to measure the fluorescence signal emitted from the solution.

Solutions of $[CuCl(bpy)_2]Cl\cdot$hydrate were prepared with *ca.* 2 mM copper concentration in saline phosphate buffer (PBS, 0.137 M NaCl, 0.01 M Na_2HPO_4, 0.002 M KH_2PO_4, 0.003 M KCl). Solutions were degassed in a MBraun Glove box and transferred to gas-tight syringes and valves (Hamilton). The three syringes, one containing supporting electrolyte, PBS, for the counter electrode (CE) and a pair of syringes for the working electrode (WE) were removed from the glove box and connected to the XAS-SEC cell. The narrow-bore 1/16” Teflon tubing was flushed with dinitrogen before connecting to the filled syringes. With appropriate fittings it is possible to establish a closed volume of cell and syringes without measurable dioxygen contamination.

Electrochemical measurements were conducted using a PalmSens4 compact electrochemical interface. The 10 V compliance voltage and 30 mA maximum current were compatible with the demands of the large-surface area WE of the XAS-SEC cell. The cell incorporated a model ET072 (eDAQ) 2 mm diameter leakless Ag/AgCl miniature reference electrode (RE) and the porous WE and CE were fashioned from 500 pores per inch reticulated vitreous carbon (RVC, Destech Corporation) which had been made hydrophilic by immersion in concentrated sulfuric acid then thoroughly rinsed with MilliQ water and buffer. The space between the electrodes was filled with glass beads (45-60 mesh, Selby).

The design criteria for the XAS-SEC cell are described in the following section and was implemented using open-source software, OpenSCAD (*OpenSCAD*, 2020). This supports the output of the STL files needed for 3D printing. A Connex3 Objet350 printer with UV-cured ink (Vero, exo-1,7,7-trimethylbicyclo[2.2.1]hept-2-yl acrylate, camphene) and water-soluble support (acrylic acid, 2-hydroxyethyl ester) produced objects with high geometric precision which are suitable for working with aqueous solutions. The UV-cured polymer was found to contain low concentrations of copper and a detectable Cu edge could be observed for direct irradiation of that material. For the cell body this does not present a significant problem since the X-ray flux after passage through the sample is attenuated to the order of 1% and any fluorescence from that source directed towards the detector will be further attenuated by the sample. The mounting plate will be exposed to scattered X-rays; fluorescence thereby excited has an unattenuated path to the detector elements and presents the most serious risk of contamination of the spectra of low concentration samples. The thermoset printing material ULTEM does not contain measurable concentrations of copper, and while unsuitable for printing the main body of the XAS-SEC cell, could be used to print satisfactorily the front mounting plate (Figure 1a). Measurements from the XAS-SEC cell with the WE containing supporting electrolyte using the cell body and CE holder printed using UV-cured polymer and the mounting plate printed from ULTEM did not give an observable copper signal. Owing to the complexity of the objects it was not practicable to program explicitly the threads when using OpenSCAD and threads were manually tapped into the printed objects. More highly featured CAD programs allow direct printing of threaded components. The technical figures for this communication were generated using the program Autodesk Fusion 360.

The physical characteristics and durability of the construction material impact on the reliability and suitability of the cell for different applications. The UV-cured polymer is rigid, but brittle, and has poor non-aqueous solvent compatibility. The internal threaded sections are vulnerable to stripping and manually tapped threads could be used for 3-4 occasions. The durability of the threaded components may be improved by additional UV-curing of the cells or by explicit printing of the threaded sections.

Thread inserts present an alternate strategy commonly used when tapped sections are needed in soft materials. That strategy would require more substantial redesign to accommodate the larger-diameter holes needed for the inserts. However, it is important to note that the limitation in repeat use of the current cell is offset by the comparatively low unit cost of the 3D-printed cell.

The four-axis stepper motor syringe pump was constructed using 0.9° JK57HM41-1006 (Changzhou JKongmotor Co., Ltd) stepper motors coupled to a 4-turn/mm lead screw (Thorlabs F6MSS100-sp). A matching threaded bushing (Thorlabs F6MSSN1P) was attached to a 20×20×100 mm^3 acrylic block. The elimination or minimisation of backlash in the flow system is a key design property as this defect can cause pressure changes in the WE and lead to a period when the solution is static when flow direction is reversed. Backlash was minimised using guide rods (8 mm diameter silver steel ground shaft rod) which were offset by 40 mm from the beam axis (Figure 2a). The mounting plates for the stepper motors, alignment guides and syringes were laser cut from 8 mm thick acrylic sheet. Further details of the construction of the syringe pump assembly are given in the supporting information, S1.

A KTA-290 USB Serial Stepper Motor Controller and SFC-027 Big Easy Driver boards were used to control the stepper motors. Purpose-built software, written using Microsoft Visual Studio, allowed control of the 4 independent syringe pumps. This supported the operation of the XAS-SEC cell in linear flow and pulsed flow modes with automatic reversal of the direction of net solution flow after reaching programmable software limits (supporting information, S2). At the highest resolution (16 microstep/step) the linear resolution is 25.8 microsteps/μm and backlash < 2 μm.

3. Results and Discussion

3.1. XAS-SEC cell

Whilst the basic principles of the design of the XAS-SEC cell have been described previously, (Best *et al.*, 2016) the coupling of CAD with 3D printing can allow the realisation of more intricate designs and inexpensive unit costs. Whilst there are a range of commercial CAD programs, open source software such as OpenSCAD (*OpenSCAD*, 2020) provide sufficient functionality to allow the design of the component parts and generation of files for printing and 3-D visualization. The STL files of the main body, CE holder and mounting plate are available in supporting information, S3.

Critical requirements for the cell design are the minimisation of the solution volume needed for operation and optimisation of the reliability of cell assembly in terms of establishing electrical connections and elimination of leaks. The electrochemical cell consists of porous WE and CE fashioned from RVC with a 2 mm diameter Ag/AgCl RE positioned with its junction close to the WE. Mixing of the solution in the WE and CE is minimised by packing the space between the electrodes with glass beads with particle size larger than the galleries in the RVC (>100 μm). While materials such as Nafion can provide ion transport while blocking diffusion of large and/or anionic species, the restrictions that this barrier provides to mass transport and, for the current design, complicates filling and flushing the flow cell. Our previous investigations (Streltsov *et al.*, 2018, Best *et al.*, 2016) suggest that after flushing the WE and flow system there is a sufficient diffusion of the solute into the glass bead layer in contact with the WE for there to be no significant variation in the solute concentration during flow experiments. The WE is enclosed by a Teflon-coated Kapton film sandwiched between the main body and the mounting plate. Leakage between the Kapton film and the cell body could be eliminated by use of a Teflon gasket, fashioned by cutting out a rectangle from Teflon tape with dimensions matching the WE slot. Electrical connections to the RVC electrodes are achieved using a graphite rod (0.9 mm HB pencil lead) which is O-ring-sealed into the main body (WE) or CE retainer using an O-ring (Figure 1a). A Nylon M4 screw with a central M2 tap is used to compress the O-ring, then an M2 screw is used to push the graphite rod into the RVC and provide electrical contact. The 1/16” tubing which facilitated solution flow through the electrodes was sealed into the XAS-SEC cell using Flangeless Liquid Chromatography fittings (Upchurch Scientific).

In operation the cell is connected to the three syringes, tested for leaks and degassed by a flow of dinitrogen. Deoxygenated supporting electrolyte is flowed into the CE entry port and out the WE inlet/outlets and the electrochemical performance of the cell tested. The supporting electrolyte in the circuit between the two WE syringes is replaced by flowing the solute solution to waste. It was found that 50 μL in addition to the dead volume of the taps, tubing and WE volume was sufficient to provide an enclosed volume which was not affected by significant concentration gradients.

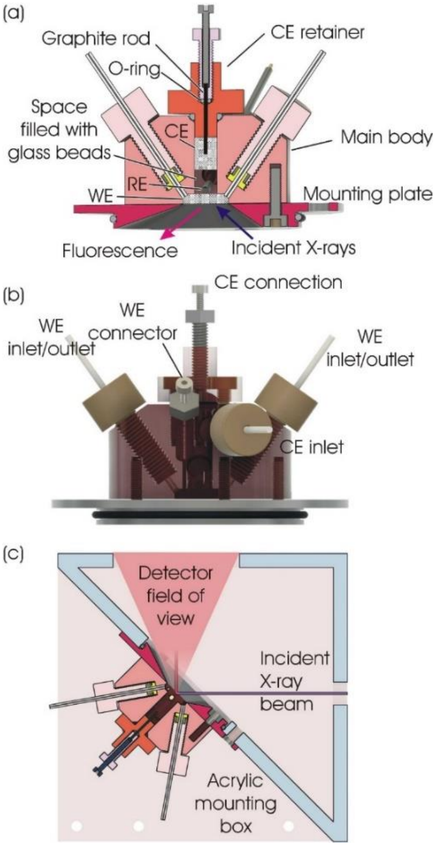

Figure 1 (a) Cross-sectional view of the XAS-SEC cell showing entry and exit ports, the positioning of the working (WE), counter (CE) and reference (RE) electrodes and the electrical connection to the CE. (b) 3D-CAD view of the assembled cell. (c) Cross-sectional view of the XAS-SEC cell mounted onto an Acrylic box which is sealed with Kapton windows and can be flushed with He and thereby minimise air scatter.

3.2. The flow system

Successful operation of the cell requires fine control over both the volume and rate of solution flow and while commercial syringe pumps can serve this purpose, there can be complications associated with programming the flow pattern, acceleration profile and synchronisation of independent syringes. By using a modular approach, it is comparatively straightforward to optimise the mechanical properties of the system and control software. The stepper motor (SM) assembly is shown in Figure 2. Successful implementation of pulsed-flow modes of operation (*vide infra*) require smooth acceleration/deceleration and minimal backlash associated with a change in flow direction.

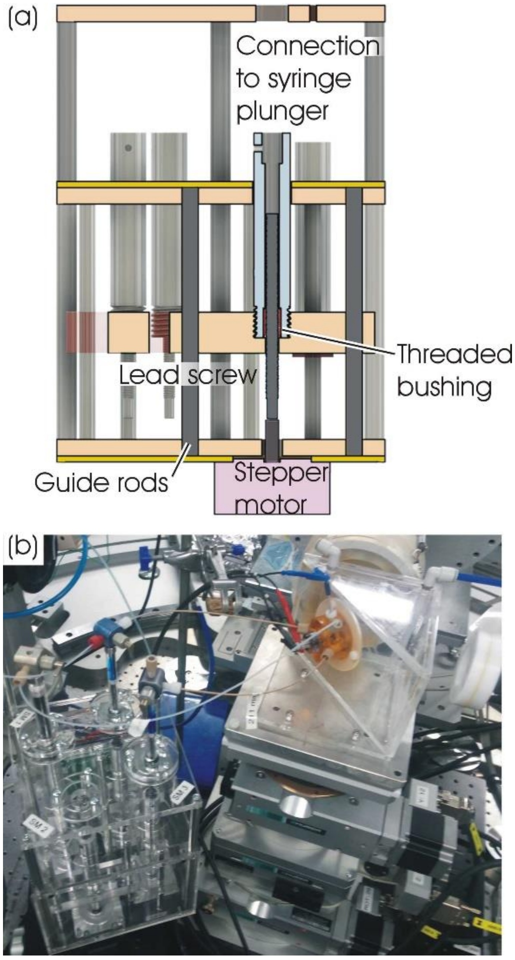

Figure 2 (a) Cross-sectional schematic diagram of a stepper motor syringe driver assembly. (b) The syringe pump assembly combined with the XAS-SEC mounted on the beamline sample stages.

Mechanical coupling of the gas-tight syringes to the SM assembly (Figure 2b) is relatively straightforward and has been optimised to facilitate coupling the syringes (supporting information, S1). In order to minimise dioxygen concentrations, the syringes are filled in a glove box and the solution isolated until the tubing and XAS-SEC cell were purged with dinitrogen gas.

A commercial 4-axis stepper motor controller with built in acceleration/deceleration and USB interface (KTA-290) provided a convenient means of controlling the stepper motors. Since the concentration needed for the collection of extended XAS spectra with good signal to noise in a reasonable timeframe (<1-2 hours) is in the mM regime, it is often challenging to obtain 1 mL of many protein samples. Consequently, solution management must be both precise and reliable. Software has been written to allow (1) the setting of software limits for each of the syringes, (2) linear flow of designated solution volumes for both an open (flow to waste) and closed (syringe to syringe transfer) configurations, (3) pulsed-flow operation of a matched pair of syringes with control over both the forward and return flow volume for each pulse and (4) reversal of the pulsed flow direction on reaching the syringe limits or the net flow if a specified volume of solution. Further details of the software are provided in supporting information, S2.

The flow properties of the sample are impacted by solution viscosity and the characteristics of the tubing used in the experiment, moreover, for large biomolecules it is necessary to ensure that the solution flow does not generate shear forces sufficient to denature the protein. The objectives of minimising the solution dead volume and the pressures within the system together contribute to the selection of the tubing. For aqueous solutions, 0.01” or 0.02” Teflon/PEEK/PEEKsil tubing has been used successfully. The introduction of air bubbles during pulsed-flow operation can be a problem and this will result from failure of the seals of the tubing or the gas-tight syringe and will be exacerbated by the negative pressures generated during pulsed flow. In addition to attention to the plumbing, it is necessary to ensure well-matched operation of syringe pumps and that the programmed flow, including the acceleration/deceleration profile, can be supported by the system.

3.3. XAS Spectroscopy

In order to minimise air scatter and to fix, reliably, the angle between incident beam and the front surface of the WE at 45°, the XAS-SEC cell was mounted onto a He-flushed acrylic box (Figure 1c). With this orientation the WE can be translated over a 5×1.2 mm^2 area while maintaining an unattenuated path of the fluorescent photons to the detector (Figure 1a). This is sufficient for a 4×2 grid of non-overlapping sampling positions of the 0.4×0.3 mm^2 beam of I20-Scanning, which may be used to assess beam-induced damage to the electrode.

Critical to the experiment design is the identification of a combination of flow and X-ray flux parameters which allow the measurement of spectra while minimising photodamage. In order to minimise the quantity of sample dedicated to this task a pulsed sample mode of operation was used and the direction of solution flow reversed after passage of a net flow of 50 – 100 µL. In this way several combinations of net flow per pulse, residence time and X-ray beam intensity can be tested. Once a suitable set of parameters are identified, and the constancy of the spectra with a lower beam flux confirmed, the cell is moved to illuminate a fresh area of the electrode and the “setup” solution flowed beyond the sampling point of the cell.

For the flowing sample photodamage to the sample does not appear to depend simply on the photon dose. If the concentration of photoredox products is maintained at a low level the photochemical reactions can be reversed by chemical or electrochemical reactions. Similar spectra could be obtained from 100 µL of solution passed through the sample point ten times as from the linear passage of 1 mL of solution with the same pulse characteristics (*i.e.* both with and without reversing the direction of net flow). There is some mixing of the solution in the syringe during the pulsing of the solution – as may be seen in cases where the redox reaction leads to a change in colour of the solution (Figure 3). The reproducibility of the spectra can be tested by (1) recovery of the starting spectrum by application of an appropriate potential and (2) repeat measurements from a “fresh” part of the solution contained within the syringe.

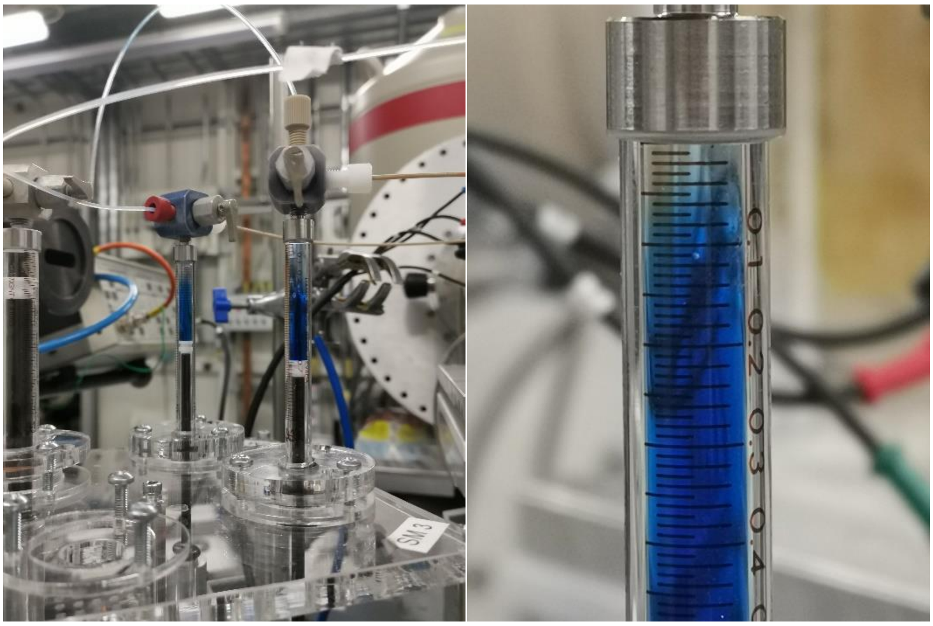

Figure 3 Solutions of a copper(II) complex together with the redox mediator DCIP (dichlorophenolindophenol) following multiple passes of 100 µL of the XAS-SEC cell at reducing potentials. The oxidised form of DCIP is an intense blue and the reduced form colourless. A closeup view of the receiver syringe is shown.

The quality of XAS data depends both on the compositional stability of the sample and the stability of cell relative to the beam. In particular, changes to the geometry of the front window of the WE due to pressure changes during pulsed flow operation will introduce higher-frequency noise into the spectra and longer timeframe distortions would be associated with any changes in the composition of the sample over the course of the measurement. We have previously established that with properly matched syringes there is no degradation of the S/N ratio for pulsed flow compared with static or linear flowing solutions (Streltsov *et al.*, 2018, Best *et al.*, 2016). The stability of the sample and the state of the electrode surface must be assessed in the context of the total measurement time, the photon flux and flow characteristics of the solution.

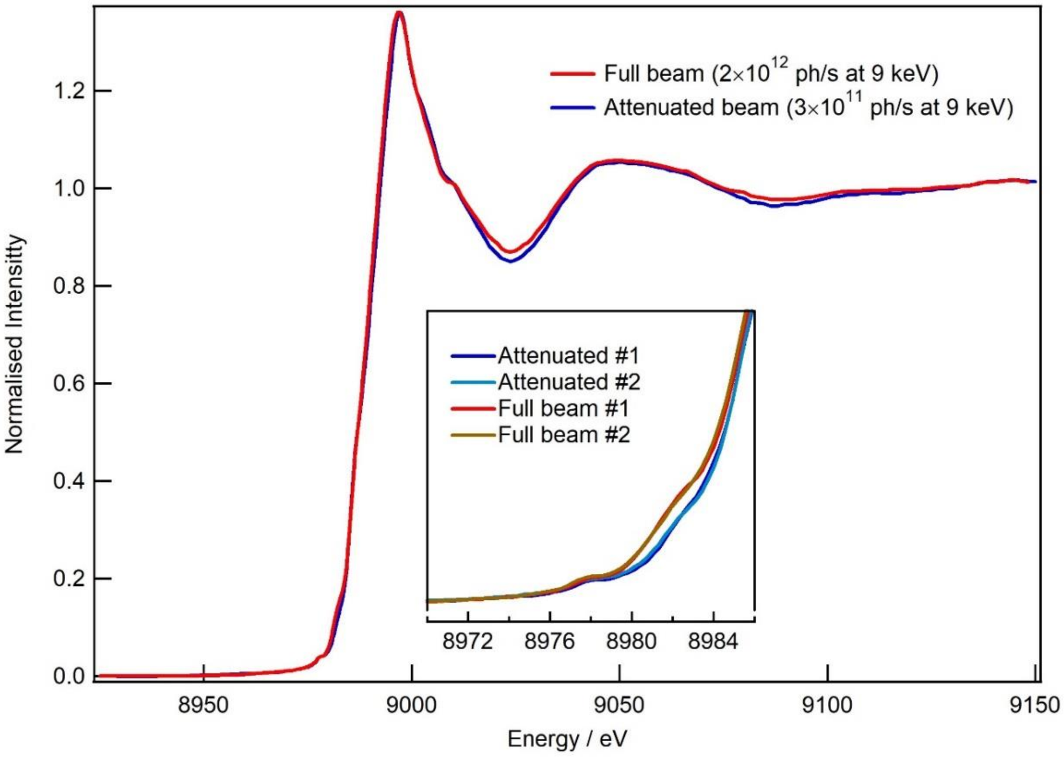

Figure 4 Power-dependence of the XANES of [CuCl(bpy)$_2$]Cl.hydrate (2 mM in PBS). Pairs of normalised spectra are shown for measurements recorded with the full beam and the beam attenuated using 0.2 mm Al foil. Further increases in beam attenuation did not result in significant spectral changes. The inset shows pairs of spectra recorded with full and attenuated beam and shows the reproducibility of the spectral changes.

For the solute species, a good starting position is to set a pulse with forward and reverse flows of 0.5 and 0.4 μL and a frequency of 2 Hz. This would give a net flow of the solution front of 1 mm in 50 s. Since the I20 scanning beam height is 20% of that of the WE, mixing of the solution during pulsing will give the solution an average exposure time of ca. 5 s for a 1 mm beam width. These flow parameters give a net flow of 100 μL of solution in 16.7 mins. Starting with a more attenuated beam, the XANES were monitored as a function of the photon flux and systematic differences in the spectra were used to set an appropriate beam flux. An example of the variation of the spectra in response to a change in beam attenuation is given for PBS solutions of [CuCl(bipy)$_2$]Cl·hydrate. The crystal structure indicates that the complex has a distorted five-coordinate geometry (Stephens & Tucker, 1973) and retention of the bound chloride in nitromethane is confirmed by conductivity measurements. The similarity of the ligand-field transitions in solution UV-Vis spectra of the salt in nitromethane (Ondrejovic *et al.*, 2002) and PBS support the retention of a distorted five coordinate geometry in both solvents. The pre-edge spectra of $[CuCl(bpy)_2]^+$ have a weak feature near 8978 eV (Figure 4), assigned to the ‘Laporte forbidden’ 1s-3d transition of copper(II) (Tomson *et al.*, 2015, DuBois *et al.*, 2000, Kau *et al.*, 1987). Photoreduction, with generation of copper(I) complexes, is associated with the appearance of the more intense 1s-4p transition, which has been reported in the range 8983-6 eV, depending on the coordination of the metal (Kau *et al.*, 1987). The increase in intensity at *ca.* 8982 eV with the unattenuated beam (Figure 4 inset) is attributed to photoreduction of $[CuCl(bpy)_2]^+$. It is noteworthy that the magnitude of the changes to the post-edge oscillations (*e.g.* at *ca.* 9020 eV) due to photoreduction are more pronounced than that of the 8982 eV feature (Figure 4).

If the maximum safe flux is insufficient for the collection of extended XAS spectra with good signal to noise, then the flow parameters can be further refined. In contrast to measurements from a static sample, the flowing solution will have a fixed, steady state composition and will be less affected by spectral distortion resulting from time-dependent changes in sample composition induced by prolonged exposure to the beam (Best *et al.*, 2016, Streltsov *et al.*, 2018).

The surfaces of the WE may be contaminated by deposition of insoluble products of electrolysis or photolysis and this can lead to significant time-dependent changes in the spectra. For metalloproteins and polypeptides this may include oligomerisation by coupling of radical species generated at the protein surface, or through protein adsorption on the electrode surface. It is common for the electrochemical response of the cell to change with increased exposure of the electrode to the protein solution. This will often be the result of adsorption of fragments of apo-protein and this will not impact significantly on the XAS spectra. The adsorption of metalloprotein will, however, have a significant adverse impact – particularly when there is adsorption at the point of exposure to the X-ray beam. While instances of this effect will generally be manifest by a continuous increase in the edge intensity with time, more subtle effects can only be checked at the end of data collection when the sample solution can be replaced by supporting electrolyte. In this case the loss of all signal from the element of interest provides confirmation that the measured spectra are not contaminated by surface-adsorbed species. Where the voltametric or spectroscopic signatures suggest possible contamination of the WE then it is important to compare the in-situ measurements with spectra obtained from solution or frozen samples that do not include the RVC WE.

3.4. Electrochemistry

As noted previously, despite the large area of the WE, reasonable electrochemical response can be obtained from XAS-SEC cells if due attention is given to ion migration and the geometry of the CE and RE (Best *et al.*, 2016). Precise control over the placement of the electrodes for the 3D printed cell allows further improvement in performance. Herein, we focus on the beam-dependent response of the

XAS-SEC cell and the insight this can give on the chemical potential of the solution under investigation during continuous illumination by ionising radiation. In a previous study it was reported that the magnitude and sign of the photoinduced current response from an electrode-adsorbed film of CoO_x in XAS-SEC experiments was sensitive to the applied potential (King *et al.*, 2019). The sign of the photocurrent was interpreted in terms of oxidation or reduction of the CoO_x film as a consequence of photoionization.

In aqueous solution photoionization leads to strongly oxidising and reducing species *viz.* aquated electrons, hydrogen and hydroxy radicals which are rapidly consumed in annihilation (*e.g.* formation of H_2 or H_2O_2) and spontaneous redox reactions with solute species (Schwarz, 1955) which include, but are not limited to, the copper complex (Anbar & Neta, 1967). In active modes of operation of the electrochemical cell, the WE will act as a redox participant and will provide a sink for both highly oxidising and reducing species and maintain the Nernst equilibrium for the chemically-reversible redox couples. The high rates of reaction of the initial products of photoionization relative to mass transport makes the WE a less probable redox partner than high-concentration solute species. Enhanced protection against photodamage of the sample by *in-situ* electrochemical approaches derives mostly from the removal of the longer-lived reactive secondary products of photoionization and the reestablishment of the Nernst equilibrium of the species of interest. Electrochemically irreversible reactions involving those species may be chemically reversed on longer exposure of the solution to the WE away from the irradiation zone and under these circumstances the sample solution may be sampled multiple times without significant change of the spectra (Streltsov *et al.*, 2018).

In open circuit operation the potential of the WE relative to the RE corresponds to the open circuit potential (OCP). This will relate to the relative concentrations and redox potentials of the solute species in contact with the WE and is a measure of the E_h of the solution. Since only *ca.* 1% of the WE is subject to illumination by ionizing radiation, the OCP will not give a quantitative measure of the E_h of the solution in the illumination zone, although the change in OCP in the absence and presence of illumination will be indicative of the change in E_h of the solution under investigation which, in turn, can be used to assess the susceptibility of the sample to oxidation or reduction during measurement.

The OCP of a 2 mM solution of $[CuCl(bpy)_2]^+$ in PBS in the XAS-SEC cell with a fresh RVC WE was *ca.* 0.35 V *vs* Ag/AgCl. The OCP is observed to be highly sensitive to exposure of the sample to the beam as illustrated by measurements obtained from the last spectrum of a series recorded with attenuated and full beam intensity (Figure 5). The OCP value depends on the ~~standing~~ concentration and chemical activity of the oxidised and reduced products and together with the conditioning of the electrode, this depends on the beam intensity and the flow properties of the solution. The negative shift of the OCP indicates more reducing conditions and is consistent with the reported proclivity of copper(II) complexes to photoreduction (Summers *et al.*, 2019, Stellato *et al.*, 2019). The response of the OCP to a change in beam intensity is reflected by the highly reproducible signature associated with the start of each scan. This coincides with a check of the alignment of the four-bounce monochromator axes during which the beam on sample is interrupted in a highly reproducible manner (Figure 5). The continued decrease in OCP on resumption of continuous illumination reflects an increased concentration of reduced species in contact with the electrode but outside the illumination zone and is a result of the net flow of the solution through the WE. As expected, these effects are more pronounced for the full beam. Closing the incident beam shutter is accompanied by an increase in the OCP which can be modelled to a double exponential decay (supporting information, S4). This is consistent with there being a combination of more short-lived products (half-life <5 s), which will be restricted to the solution under illumination, and longer lived products (half-life > 40 s), which will be more dispersed within the WE. For measurements with a higher photon flux the decay results in a more negative value of the OCP, suggesting a greater change in the composition of the solution as a result of irreversible chemical reactions. While the available measurements do not allow a more quantitative interpretation of the OCP measurements, they do highlight the potential that such measurements can provide for understanding the sensitivity of solution samples to photoionization and to assess the impact of additives such as cryoprotectants or redox mediators on the redox stability of the solution.

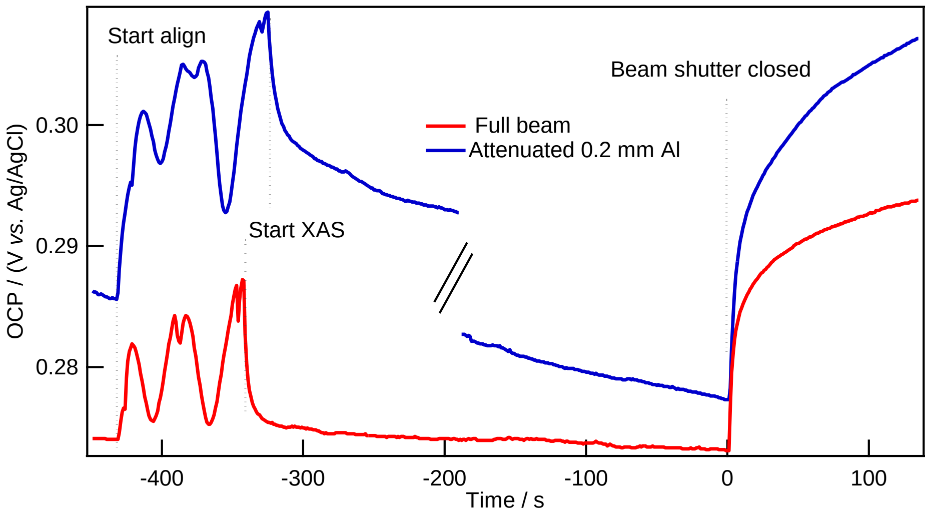

Figure 5 Variation of the open circuit potential (OCP) with time during measurement of the XANES of $[CuCl(bpy)_2]^+$ (Figure 4) The time scale for the full beam trace was adjusted so that the shutter is closed at time = 0 s. Prior to the start of each scan the alignment of the four-bounce monochromator axes is checked, and this gives a reproducible set of variations in the beam intensity. A wider scan range was applied for the attenuated beam scan. The start and end of the full and attenuated beam measurements were aligned by extracting a block of measurements during the longer attenuated beam scan. The full OCP data for the attenuated beam measurements and a more detailed description of the monochromator alignment routine is given in supporting information, S4.

4. Conclusions

The developments in the cell design and implementation of XAS-SEC techniques have led to significant improvements in the electrochemical performance, reliability, minimisation of sample volume and quality of the resulting XAS spectra. Key to the successful implementation of the approach is the control of solution flow through the WE/sample cell. Optimisation of the pulse stroke and net flow rate parameters and beam intensity allow the collection of high-quality spectra from comparatively modest solution volumes. The electrochemical cell provides control over both the relative concentrations of the redox forms of the sample and a sink for strongly oxidised and reduced species formed following photoionization and, in this way, can ‘heal’ the sample following exposure to the X-ray beam. Following optimisation of the flow parameters it is possible to flow a small volume (*e.g.* 100 μL) of the solution repeatedly (>10 times, over a period of several hours) through the WE without significant change to the spectra and this allows measurement from solution volumes as low as 600 μL.

While XAS-SEC measurements are undoubtedly more demanding than those conducted from frozen solutions, there are significant payoffs in terms of identification, minimisation and control of photoreduction as well as control over the redox state. Moreover, interference from Bragg peaks – a persistent blight of cryogenic measurements – is absent for solution samples. The measurement is dynamic – the spectroscopic response to changes of potential, solution flow and photon flux feed into experiment design and better connect to the chemistry of the system. Finally, there is, of course, a significant advantage to be gained by conducting measurements from systems with acid or base functionality, such as metalloproteins, with control over both the pH and temperature.

The advances in 3D printing and more general accessibility to commercial printing and computer-controlled machining and cutting services have brought low-volume purpose designed and built apparatus into easy reach for researchers not blessed by unlimited budgets or subsidised workshops. The current publication provides details needed for construction and operation of the apparatus for XAS-SEC measurements. The opportunity to refine and easily test design modifications allows the optimisation of experiments which it is hoped will contribute to the study of more challenging systems.

Acknowledgements This work was carried out with the support of the Diamond Light Source, instrument I20-Scanning (proposals SP20589 and SP23523). SPB thanks Michael Zammit, Alexandre Tolotchkov the Science Faculty workshop for expert technical assistance with the mechanical and electronic equipment and Oktay Balkis and the mechanical workshop of the University of Melbourne for assistance with 3D printing and laser cutting. The opensource program OpenSCAD provided a path to development of the 3D-printed cells and we are grateful for the availability of that resource. During the experiment we benefitted from the technical support provided by the Spectroscopy group technicians and, in particular, by Darren Neville. CTC gratefully acknowledges the University of Melbourne for a grant which includes travel support. SPB and VAS gratefully acknowledge travel funding provided by the International Synchrotron Access Program (ISAP) managed by the Australian Synchrotron, part of ANSTO, and funded by the Australian Government.

References

Anbar, M. & Neta, P. (1967). *Int. J. Appl. Radiat. Isot.* **18**, 493-523.
Best, S. P., Levina, A., Glover, C., Johannessen, B., Kappen, P. & Lay, P. A. (2016). *J. Synch. Rad.* **23**, 743-750.
Bourke, J. D., Islam, M. T., Best, S. P., Tran, C. Q., Wang, F. & Chantler, C. T. (2016). *J. Phys. Chem. Lett.* **7**, 2792-2796.
Bunker, G. (2010). *Introduction to XAFS: A Practical Guide to X-ray Absorption Fine Structure Spectroscopy*. Cambridge: Cambridge University Press.
Chatterjee, R., Weninger, C., Loukianov, A., Gul, S., Fuller, F. D., Cheah, M. H., Fransson, T., Pham, C. C., Nelson, S., Song, S., Britz, A., Messinger, J., Bergmann, U., Alonso-Mori, R., Yachandra, V. K., Kern, J. & Yano, J. (2019). *J. Synchrotron Radiat.* **26**, 1716-1724.
Cotelesage, J. J. H., Pushie, M. J., Grochulski, P., Pickering, I. J. & George, G. N. (2012). *J. Inorg. Biochem.* **115**, 127-137.
Dennis, G., Helsby, W., Omar, D., Horswell, I., Tartoni, N., Hayama, S., Mikulska, I. & Diaz-Moreno, S. (2019). *AIP Conference Proceedings* **2054**, 060065.
Diaz-Moreno, S., Amboage, M., Basham, M., Boada, R., Bricknell, N. E., Cibin, G., Cobb, T. M., Filik, J., Freeman, A., Geraki, K., Gianolio, D., Hayama, S., Ignatyev, K., Keenan, L., Mikulska, I., Mosselmans, J. F. W., Mudd, J. J. & Parry, S. A. (2018). *Journal of Synchrotron Radiation* **25**, 998-1009.
DuBois, J. L., Mukherjee, P., Stack, T. D. P., Hedman, B., Solomon, E. I. & Hodgson, K. O. (2000). *J. Am. Chem. Soc.* **122**, 5775-5787.
Frenkel, A. I. & van Bokhoven, J. A. (2014). *J. Synchrotron Radiat.* **21**, 1084-1089.
George, G. N., Pickering, I. J., Pushie, M. J., Nienaber, K., Hackett, M. J., Ascone, I., Hedman, B., Hodgson, K. O., Aitken, J. B., Levina, A., Glover, C. & Lay, P. A. (2012). *J. Synchrotron Radiat.* **19**, 875-886.
Grunwaldt, J.-D. & Clausen, B. S. (2002). *Top. Catal.* **18**, 37-43.
Hayama, S., Duller, G., Sutter, J. P., Amboage, M., Boada, R., Freeman, A., Keenan, L., Nutter, B., Cahill, L., Leicester, P., Kemp, B., Rubies, N. & Diaz-Moreno, S. (2018). *Journal of Synchrotron Radiation* **25**, 1556-1564.
Kau, L. S., Spira-Solomon, D. J., Penner-Hahn, J. E., Hodgson, K. O. & Solomon, E. I. (1987). *J. Am. Chem. Soc.* **109**, 6433-6442.
King, H. J., Fournier, M., Bonke, S. A., Seeman, E., Chatti, M., Jumabekov, A. N., Johannessen, B., Kappen, P., Simonov, A. N. & Hocking, R. K. (2019). *The Journal of Physical Chemistry C* **123**, 28533-28549.
Kubin, M., Guo, M., Ekimova, M., Baker, M. L., Kroll, T., Kaellman, E., Kern, J., Yachandra, V. K., Yano, J., Nibbering, E. T. J., Lundberg, M. & Wernet, P. (2018). *Inorg. Chem.* **57**, 5449-5462.
Ondrejovic, G., Kotocova, A. & Valigura, D. (2002). *Chem. Pap.* **56**, 168-173.
OpenSCAD, (2020). http://www.openscad.org/index.html.
Parsons, J. G., Aldrich, M. V. & Gardea-Torresdey, J. L. (2002). *Appl. Spectrosc. Rev.* **37**, 187-222.
Schalken, M. J. & Chantler, C. T. (2018). *J. Synchrotron Radiat.* **25**, 920-934.
Schultz, F. A., Feldman, B. J., Gheller, S. F., Newton, W. E., Hedman, B., Frank, P. & Hodgson, K. O. (1993). *Proc. - Electrochem. Soc.* **93-11**, 108-117.
Schwarz, H. A. (1955). *Journal of the American Chemical Society* **77**, 4960-4964.
Shima, S., Pilak, O., Vogt, S., Schick, M., Stagni, M. S., Meyer-Klaucke, W., Warkentin, E., Thauer, R. K. & Ermler, U. (2008). *Science (Washington, DC, U. S.)* **321**, 572-575.
Stellato, F., Chiaraluce, R., Consalvi, V., De Santis, E., La Penna, G., Proux, O., Rossi, G. & Morante, S. (2019). *Metallomics* **11**, 1401-1410.
Stephens, F. S. & Tucker, P. A. (1973). *J. Chem. Soc., Dalton Trans.* 2293-2297.
Streltsov, V. A., Ekanayake, R. S. K., Drew, S. C., Chantler, C. T. & Best, S. P. (2018). *Inorg. Chem.* **57**, 11422-11435.
Streltsov, V. A., Titmuss, S. J., Epa, V. C., Barnham, K. J., Masters, C. L. & Varghese, J. N. (2008). *Biophys J* **95**, 3447-3456.
Summers, K. L., Schilling, K. M., Roseman, G., Markham, K. A., Dolgova, N. V., Kroll, T., Sokaras, D., Millhauser, G. L., Pickering, I. J. & George, G. N. (2019). *Inorg. Chem.* **58**, 6294-6311.
Tamura, H., Salomone-Stagni, M., Fujishiro, T., Warkentin, E., Meyer-Klaucke, W., Ermler, U. & Shima, S. (2013). *Angew. Chem., Int. Ed.* **52**, 9656-9659.
Tomson, N. C., Williams, K. D., Dai, X., Sproules, S., De Beer, S., Warren, T. H. & Wieghardt, K. (2015). *Chem. Sci.* **6**, 2474-2487.
Trevorah, R. M., Chantler, C. T. & Schalken, M. J. (2020). *J. Phys. Chem. A* **124**, 1634-1647.
Zhang, H. H., Hedman, B. & Hodgson, K. O. (1999). pp. 513-554. John Wiley & Sons, Inc.
Zhang, L. (2019). *Methods Mol. Biol. (N. Y., NY, U. S.)* **1876**, 179-195.

Supporting information

S1. Outline of the layout and elements of the stepper motor drive assembly

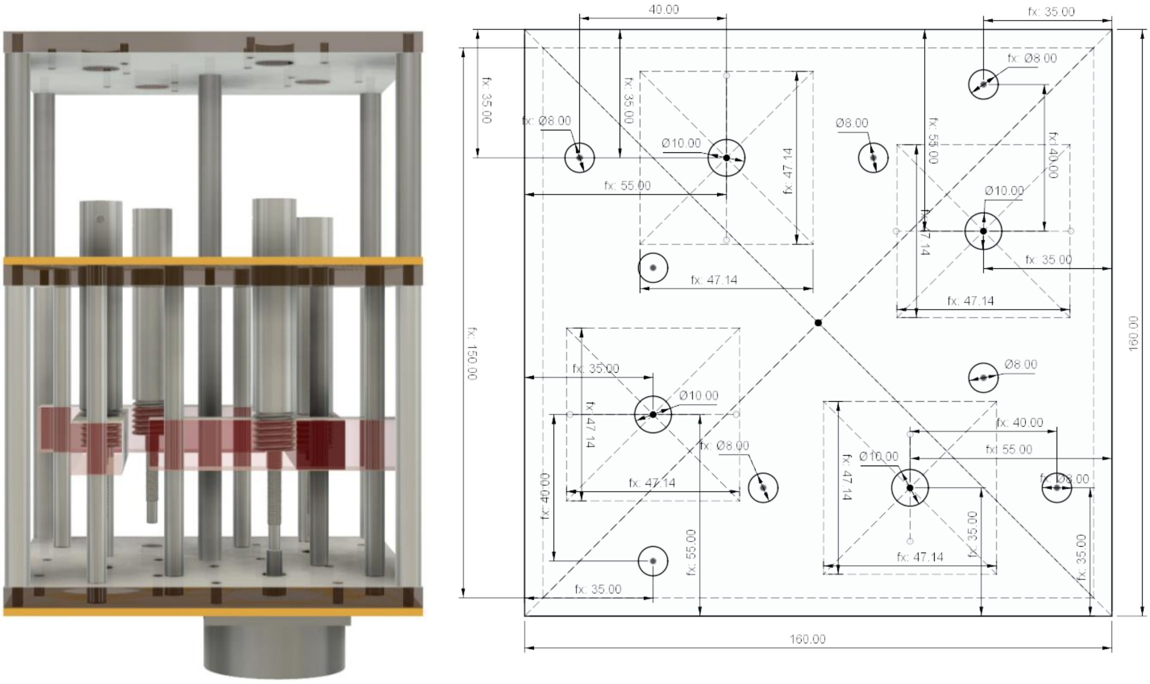

Figure S1 3D CAD representations of the 4-position stepper motor assembly (Left) and technical drawing of the layout of the bottom layer of the assembly (Right).

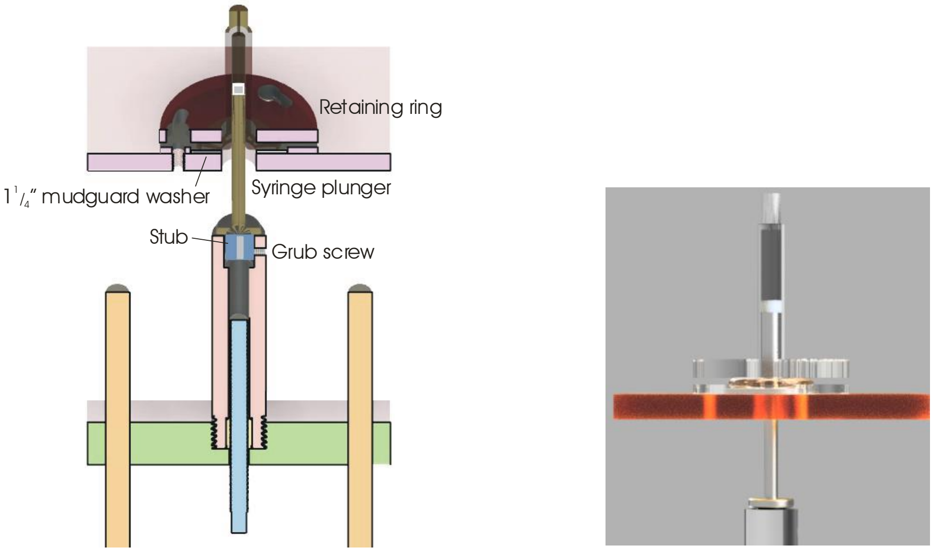

Figure S2 Details of the attachment of the gas-tight syringe to the stepper motor drive assembly. Cross-section view (left) and CAD rendered view (Right). The flanged part of the syringe barrel is tethered to the top layer of the assembly by clamping between a washer and retaining ring.

S2. Stepper Motor Controller Program

The KTA290 stepper motor controller is operated through a USB port and supports the simultaneous control of up to 4 axes. The control program needs to satisfy at least 3 functions. (1) Establish software limits based on the syringe capacity and fill state. (2) Facilitate a linear flow with a controlled flow rate and volume, including contained flow between syringes in a closed system. (3) Support pulsed flow in a closed system with control over the outward and return flow volumes, cessation of flow or reversal of the net flow direction in reaching a specified net flow volume.

The implementation of these functions is illustrated with reference to the forms comprising the relevant functions in the application.

The main window (Figure S3) provides information on the status of the stepper motors and a summary of the hardware and certain commands sent to and from the controller.

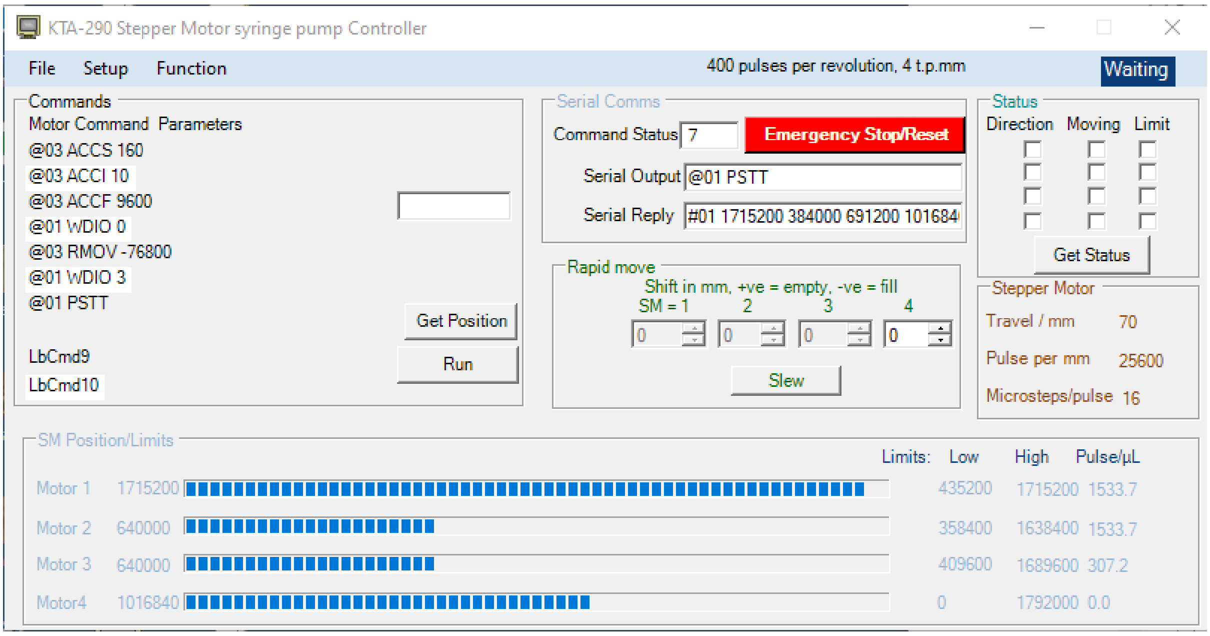

400 pulses per revolution, 4 t.p.mm

Motor Command Parameters
@03 ACCS 160
@03 ACCI 10
@03 ACCF 9600
@01 WDIO 0
@03 RMOV -76800
@01 WDIO 3
@01 PSTT

LbCmd9
LbCmd10

Command Status 7
Serial Output @01 PSTT
Serial Reply #01 1715200 384000 691200 101684

Shift in mm, +ve = empty, -ve = fill
SM = 1 0
2 0
3 0
4 0

Travel / mm 70
Pulse per mm 25600
Microsteps/pulse 16

		Limits: Low	High	Pulse/µL
Motor 1	1715200	435200	1715200	1533.7
Motor 2	640000	358400	1638400	1533.7
Motor 3	640000	409600	1689600	307.2
Motor4	1016840	0	1792000	0.0

Figure S3 The main menu

The physical limits of translation of the syringe plunger are set in the SetSyringe form (Figure S4). The syringe size, initial solution volume, maximum solution volume and projection of the plunger beyond the body of the syringe need to be associated with the syringe positions. Further, since slewing of the motors are inactivated when a syringe is set, a flag identifies whether a syringe is set at the syringe positions. Once set the low and high limits of movement and the number of pulses per µL are updated in the main menu.

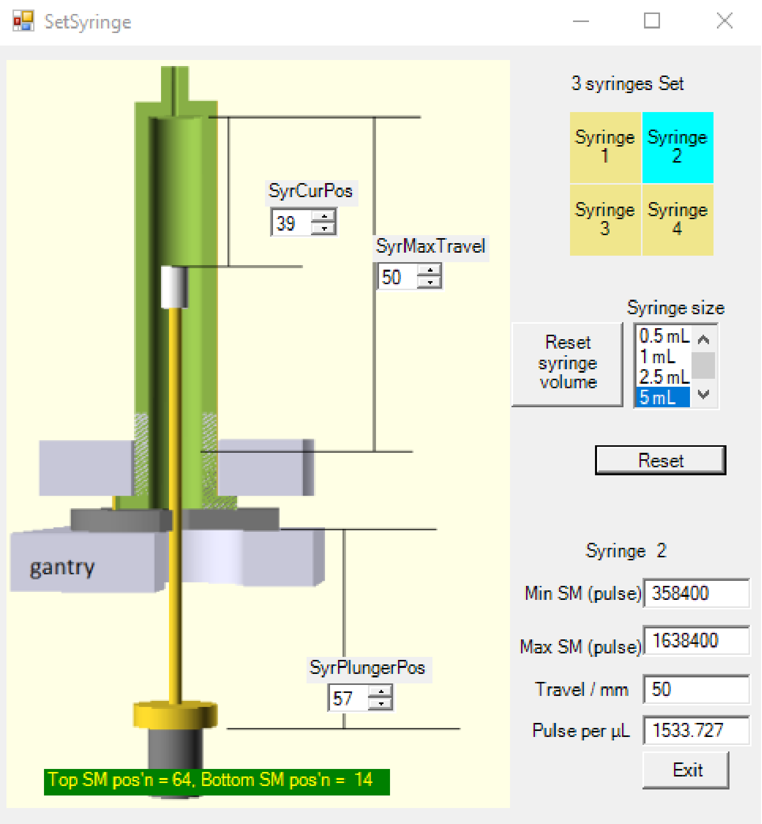

SyrCurPos 39

SyrMaxTravel 50

SyrPlungerPos 57

Top SM pos'n = 64, Bottom SM pos'n = 14

Syringe 2

Min SM (pulse) 358400

Max SM (pulse) 1638400

Travel / mm 50

Pulse per µL 1533.727

Figure S4 The form used to input the properties of the syringes attached to the syringe driver.

The flow form (Figure S5) facilitates translation of the plunger of one or more syringes at a specified velocity in terms of the number of stepper motor pulses per second. If a syringe has been set for the selected motor then the number of seconds needed to flow 1 µL is reported. Simultaneous flow of the syringes is maintained either until a specified translation of the plunger or a volume of solution (if a syringe has been set) is complete. The program will adjust the end point so as to be consistent with the low and high limits of movement given in the main menu. The stepper motor controller supports different flow rates and end times for the individual axes and it is straightforward to flow in the solution between syringes in a closed system.

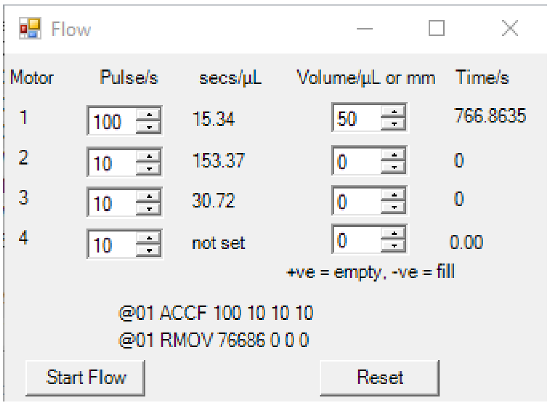

Motor	Pulse/s	secs/µL	Volume/µL or mm	Time/s
1	100	15.34	50	766.8635
2	10	153.37	0	0
3	10	30.72	0	0
4	10	not set	0	0.00

+ve = empty, -ve = fill

```
@01 ACCF 100 10 10 10
@01 RMOV 76686 0 0 0
```

Figure S5 The form used to control linear flow of the solutions.

The pulsed flow menu (Figure S6) allows flow between matched syringes. When a syringe is set the source and receiver radar items are activated and the number of stepper motor pulses per µL is reported, allowing identification of matched syringes. The pulse width corresponds to the forward flow volume (in nL) and the net flow is adjustable between 0 and the pulse width. The pulsed flow will continue in the set direction until the limit is reached with either syringe. If the reverse flow on the limit box is checked then the pulsed flow will continue, but with the definitions of the source and receiver syringes reversed. If the Use current as limit box is checked then the reversed flow will continue until the current syringe position is reached. The limit flow check box will allow the setting of the flow limits to a specified volume (*e.g.* 100 µL). In this case the current position is set as one limit and the other is set according to the net volume flow.

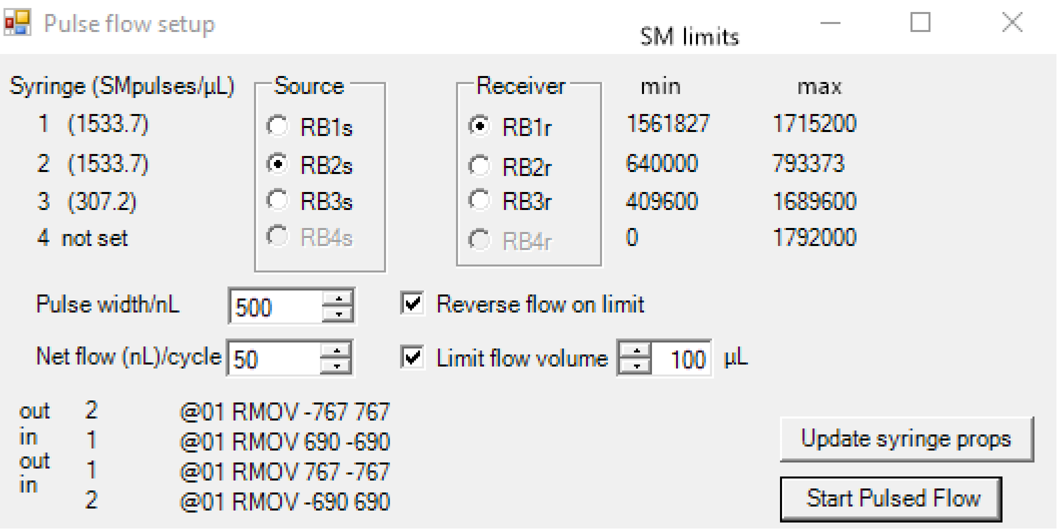

Syringe (SMpulses/µL)	Source	Receiver	min	max
1 (1533.7)	○ RB1s	● RB1r	1561827	1715200
2 (1533.7)	● RB2s	○ RB2r	640000	793373
3 (307.2)	○ RB3s	○ RB3r	409600	1689600
4 not set	○ RB4s	○ RB4r	0	1792000

Pulse width/nL 500
Net flow (nL)/cycle 50
☑ Reverse flow on limit
☑ Limit flow volume 100 µL

```
out   2   @01 RMOV -767 767
in    1   @01 RMOV 690 -690
out   1   @01 RMOV 767 -767
in    2   @01 RMOV -690 690
```

Figure S6 The form used to setup the pulsed flow mode of operation.

S3. 3D Files (STL format generated using OpenSCAD) suitable for 3D printing the XAS-SEC cell.

Table S1 Details of the STL files available for download

Component	Filename	Filesize	Image
Cell body	RT-XAS-SECell_body.stl	6.15 MB	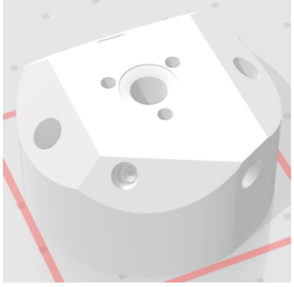
Counter electrode holder	RT-XAS-SECell_counter.stl	1.45 MB	
Front window	RT-XAS-SECell_front.stl	3.75 MB	

Note that straight holes are printed of a diameter suitable for tapping.

S4. Variation of the open circuit potential (OCP) during XAS measurements at the I20-scanning beamline of the DLS

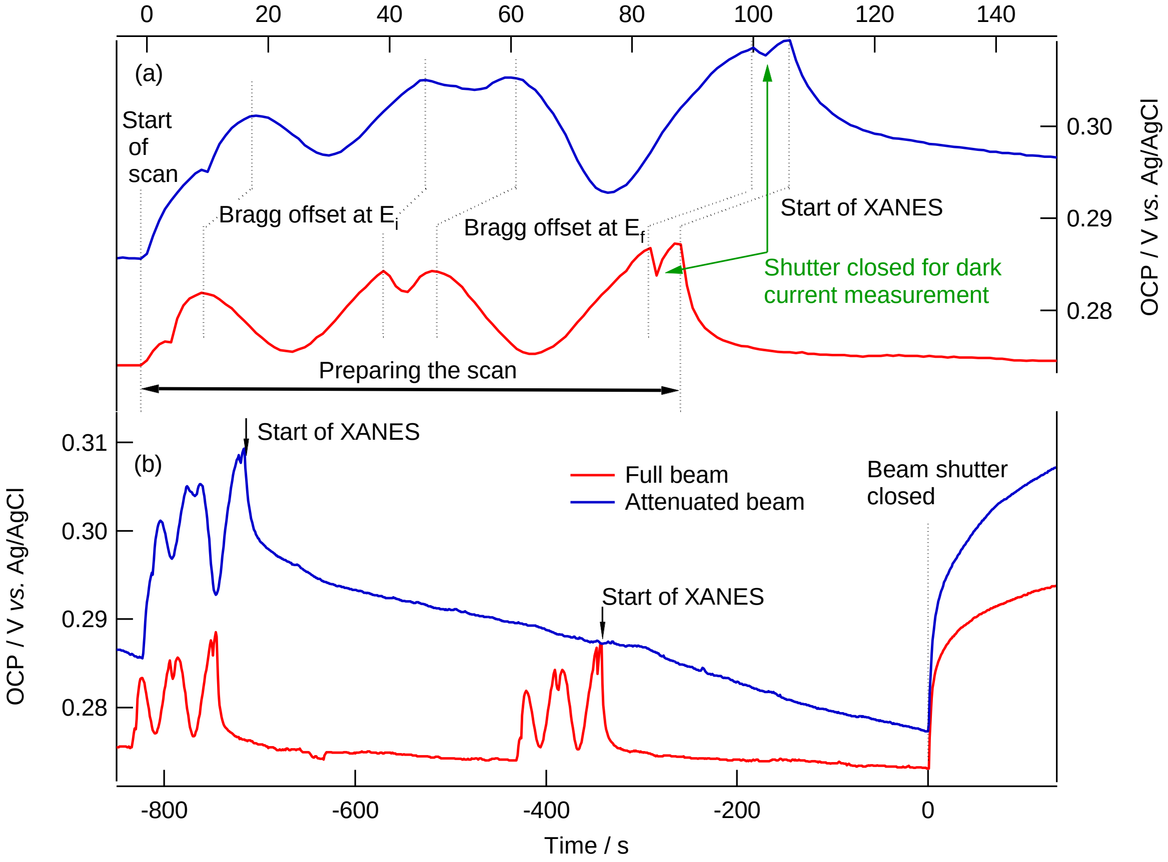

Figure S7 Variation of the open circuit potential (OCP) with time during measurement of the XANES of $[CuCl(bpy)_2]^+$. (a) expanded view during the monochromator alignment protocol and dark current measurements. During this procedure the shutter is open and the monochromator moved to the start of the scan, then the second downstream axis is scanned with respect to the upstream axis to identify the optimal alignment setting. This procedure is repeated at the end of the scan energy. During this alignment process the transmission of X-rays through the monochromator is changing and only at the maximum when the two Bragg axes are in alignment. This is reflected by the dip in the OCP. The different scan range for the full beam and attenuated beam experiments is responsible for difference in alignment time. (b) The OCP response for the full and attenuated beam scans as shown in Figure 5. In this plot the full set of data for the attenuated beam scan (XANES and EXAFS regions) is given. Approximately two XANES scans (full beam) were recorded over this timescale.

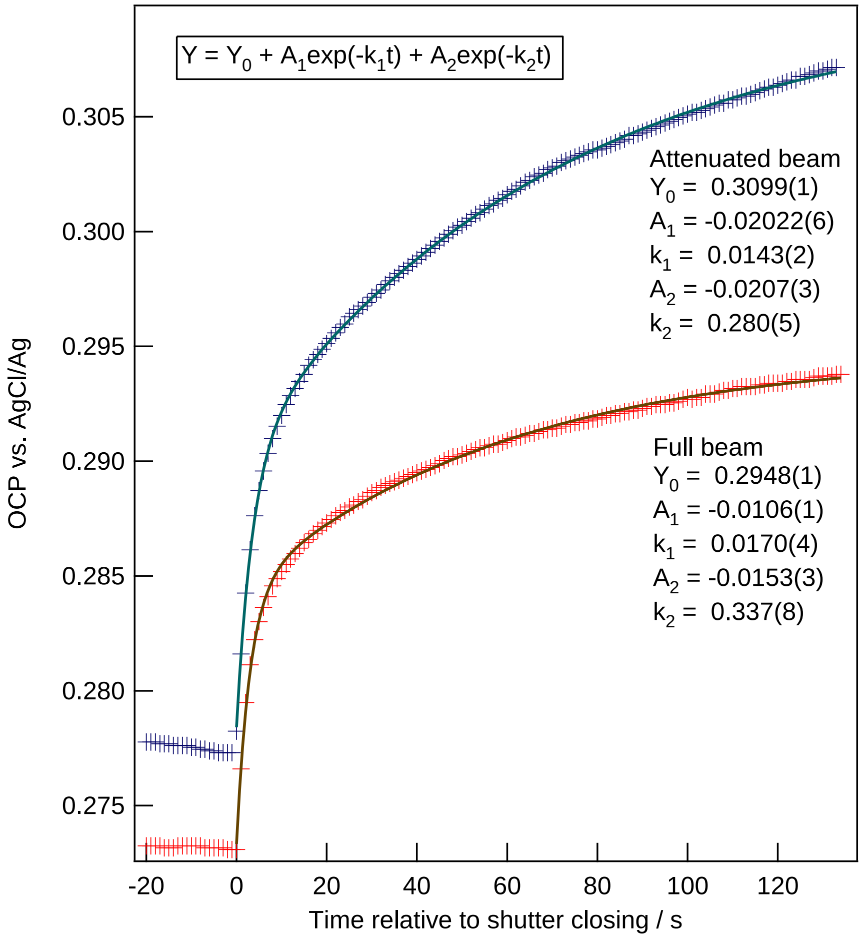

Figure S8 Fit of the changes in OCP in response to closing the shutter at the end of the scan. The decay is fitted to a double exponential using IgorPro software (Wavemetrics). The fitting function, refined parameters and estimated standard deviations are included in the figure.